Measurement and Modeling of Dynamic Rolling Friction in Linear Microball Bearings

Xiaobo Tan
Department of Electrical & Computer Engineering,
Michigan State University,
East Lansing, MI 48824
e-mail: xbtan@msu.edu

Alireza Modafe
e-mail: modafe@glue.umd.edu

Reza Ghodssi
e-mail: ghodssi@glue.umd.edu

Department of Electrical & Computer Engineering,
and Institute for Systems Research,
University of Maryland,
College Park, MD 20742

In prior work of the authors and co-workers, a vision-based system was developed for characterizing the tribological behavior of silicon-micromachined linear microball bearings. Plain difference methods introduce amplitude and/or phase distortion in computing the derivative signals (e.g., velocity and acceleration) based on the position snapshots. In this paper frequency-dependent amplitude and phase compensation algorithms are developed for both the forward difference and the central difference methods to retrieve without distortion the friction and the relative velocity between bearing elements. Processing of experimental data with these techniques reveals nonlinear, viscous frictional behavior in the bearing. A viscoelastic model based on a continuum of mass-spring-damper elements is then proposed for the ball-groove interaction. Numerical results show that this model captures the nonlinear velocity dependence of the rolling friction observed in experiments. [DOI: 10.1115/1.2362786]

1 Introduction

Bearing and support structures play important roles in micromachines (e.g., microengines, micromotors, and microgenerators) due to their implications for efficiency (friction), reliability, and complexity in fabrication and control. Typical contact-type bearings, such as the center-pin bearing with sliding bushing [1], suffered drastically from friction and wear. On the other hand, noncontact bearings, like electrostatic [2] or pressurized air levitation [3] mechanisms, show much less friction and almost no wear but require complicated fabrication steps and are hard to control. Silicon micromachined microball bearings can potentially provide simple, low-friction, and robust support in micromachines. Like their macroscopic counterparts, MEMS-based microball bearings are expected to exhibit low friction. But the effective design and control of micromachines using such bearings will demand careful characterization and modeling of their frictional behavior.

Frictional phenomena at micro/nano scales have been a subject of active research. Several approaches were reported including, e.g., measurement with atomic force microscopes or frictional force microscopes [4,5] and in situ direct measurement using micromachined structures [6–9]. Most of studies, however, was focused on static or dynamic friction in sliding instead of rolling. A linear microball bearing structure was proposed and its static coefficient of friction (COF) measured by Ghodssi et al. [10]. Its dynamic COF was investigated with a vision-based experimental setup [11], where a Coulomb friction model was used. Recently the authors and their co-workers upgraded the experimental system to capture motions of all bearing elements (the slider, the stator, and the microballs) with infrared imaging. This led to characterization of some important tribological behaviors [12]. However, a faithful model is still lacking for the microball bearings since the Coulomb model was a crude approximation, as evidenced by the scattering of data points on the friction versus velocity plot [11].

Classical frictional models typically express the frictional force as a static function of the relative velocity between the contact surfaces, which may include the static friction, Coulomb friction, Stribeck friction, and viscous friction [13,14]. The Dahl model describes the friction in the presliding regime in terms of the micro-displacement [15]. The relationship between the friction and the displacement can be hysteretic [16]. A dynamic friction model (called the LuGre model) was presented by Canudas de Wit et al. with an internal state representing the average deflection of contacting asperities [17], and was further extended by others [16,18]. This model demonstrated, among other properties, the hysteresis between the friction and the sliding velocity for unidirectional sliding. Such hysteresis was also reported for unidirectional, unsteady sliding velocities and modeled through a time lag by Hess et al. [19]. Similar hysteresis behavior was studied for a forced oscillator with a compliant contact [20]. The experimental results reported in [16,17,19,20] were all based on macroscopic systems.

This paper aims to model the dynamic friction in linear microball bearings consisting of micromachined silicon V-grooves and commercially available stainless-steel microballs. These bearings can be used in linear micromotors with application to long-range, precision micropositioning. The term "dynamic friction" (as opposed to the *static friction*) refers to the friction when a relative motion between the slider and the stator is present. In the experiment the stator is fixed to a forced oscillator, and the motion of the slider is driven only by the friction. Hence the friction is directly linked to the acceleration of the slider, which is determined based on successive video images. In general, the bearing dynamics is very complex due to fabrication-related surface irregularities, ball-to-ball or ball-to-wall collisions, and oxide growth on contact surfaces [12], and the slider may occasionally demonstrate stick-slip, slow drift, or sudden impacts. However, the emphasis of this paper is on the frictional behavior when the slider is (relatively) steadily sliding, which would be the normal operating condition once the fabrication processes are refined. Due to the constraint of camera speed, the (relative) velocity regime is about $[-0.02, 0.02]$ m/s. Note that this limitation does not undermine the importance of the study since interesting friction-related dynamics typically takes place at low velocities and during velocity reversals.

In the vision-based measurement system both the friction and the (relative) velocity are derived from the position information available through the camera. Finite difference methods are commonly used to obtain approximations of derivatives, including approximations of the velocity and the acceleration from the displacement data [21]. Efforts have been made to reduce the
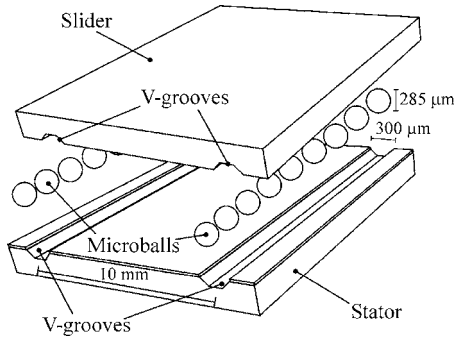
Fig. 1 Schematic of a linear microball bearing [11]

Fig. 2 Vision-based experimental setup

approximation errors through, e.g., the development of high-order methods [22,23]. In this paper algorithms are developed to fully compensate the distortion by exploiting the periodic nature of the signals involved. The distortions in amplitude/phase introduced by the forward difference and the central difference methods are first derived for sinusoidal signals. Since the actual signals contain high-order harmonics, fast Fourier transform (FFT) is conducted to isolate individual frequency components for subsequent compensation.

Both numerical and experimental results show that the algorithms can effectively recover the derivative quantities based on the position snapshots. Processing of the experimental data shows that (at least for the velocity range considered in the paper) the friction is a static function of the velocity. At low relative velocities, the friction is approximately linear in the relative velocity, thus demonstrating a viscous behavior; as the relative velocity increases, the friction approaches saturation and then shows a dropping trend upon further increase of the velocity. For simulation purposes, a Langevin function is used to approximate the friction-velocity relationship. The predictions of the slider amplitude and the slider/state phase difference based on this empirical model agree well with the experimental results.

A viscoelastic model is further proposed to explain the observed behavior. A large body of literature is available on stress/strain analysis for rolling contacts including frictional contacts (see, e.g., [24–27]). Inspired by the work of Poschel et al. on rolling friction of a hard cylinder on a viscous plane [28], we model the groove plane as a continuum of mass-spring-damper elements with the masses moving perpendicular to the plane. The distinction is that the 3D geometry needs to be addressed here while a 2D geometry was considered in [28]. Moreover, the comparable hardness demonstrated by silicon [29] and steel entails appropriate modification of the assumption of a hard body rolling on a viscous plane. Given a rolling velocity, the penetration depth of the ball into the groove plane is determined through an implicit equation of force balance and can be solved for by the fixed-point iteration algorithm. The mechanical power required to actuate the continuum of mass-spring-dampers is then calculated, from which the rolling resistance (friction) is derived. Numerical calculations show that this model is able to reproduce the nonlinear, velocity-dependent behavior of the rolling friction observed in experiments.

The remainder of the paper is organized as follows. The linear microball bearing and the vision-based measurement system are described in Sec. 2. The data processing algorithm is presented in Sec. 3. The algorithm is applied to experimental data and the empirical friction-velocity relationship is revealed in Sec. 4. In Sec. 5 the viscoelastic model is introduced and comparison with experimental results is reported. In Sec. 6 concluding remarks are provided.

2 Experimental Setup

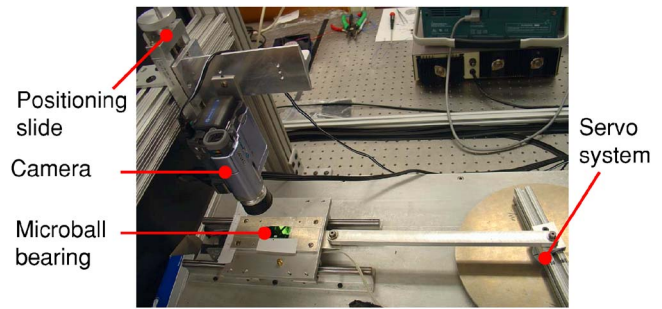A schematic of a linear microball bearing is shown in Fig. 1.

The bearing consists of two silicon plates (slider and stator) and stainless-steel microballs of diameter 285 μm. Two parallel V-grooves, which house the balls, are etched on the plates using potassium hydroxide (KOH) solution. Figure 2 shows the picture of the experimental setup. The stator of the bearing is mounted on an oscillating platform driven by a servomotor through a "crank-slider" mechanism (for more details, see [11]). The platform (and hence the stator) moves only in the direction of the underneath guiding rails and so does the slider of the bearing. The position of the stator is *approximately*

$$x_{stat}(t) = X_{stat} \sin(\omega t) \tag{1}$$

where ω is the angular velocity of the servomotor, and the oscillating amplitude X_{stat} can be adjusted. Distinct marks are placed and also etched on the stator and slider of the bearing, respectively. A CCD camera (Sony DCR-TRV22) with a 24× magnification lens captures motions of these marks, and position information of the slider and the stator can be extracted through image processing.

3 Compensation Algorithms for Difference Methods

The equation of motion for the slider is:

$$M_{slid}a_{slid}(t) = F_{fric}(t) \tag{2}$$

Here M_{slid} denotes the mass of the slider, $a_{slid} \overset{\triangle}{=} \ddot{x}_{slid}(t)$ denotes its acceleration, and F_{fric} is the friction between the stator and the slider. The slider experiences periodic motion during steady sliding. To determine whether there is hysteresis or other memory effect in the friction versus relative velocity relationship, one can check the phase difference between a_{slid} and v_{rel}, where v_{rel} denotes the relative velocity:

$$v_{rel}(t) = v_{slid}(t) - v_{stat}(t) = \dot{x}_{slid}(t) - \dot{x}_{stat}(t)$$

If the phase difference is a multiple of π, a_{slid} will be a static (memoryless) function of v_{rel}, and it will be a dynamic or hysteretic function of v_{rel} otherwise. Note that due to the nonlinearity of friction, each of x_{slid}, v_{slid}, v_{rel}, and a_{slid} will typically contain more than one frequency component. Therefore, one needs to look at their fundamental frequency components when calculating the phase difference.

A challenging problem here is that all derivative quantities, $a_{slid}(t), v_{slid}(t), v_{stat}(t)$, and $v_{rel}(t)$, can only be obtained through finite differencing of noisy position *snapshots*, $x_{slid}[n]$ and $x_{stat}[n]$ (note that, in practice, $x_{stat}[n]$ is also extracted through image processing instead of being calculated from (1)). Plain difference methods introduce distortions to the true derivative signals. In order to compensate for these errors, the amplitude scaling (and phase shift if applicable) for sinusoidal signals is first quantified for two commonly used finite difference methods.

3.1 Distortion Induced by Finite Difference Methods. The analysis is conducted for a generic sinusoidal function $x(t) = X \sin(\omega t + \phi)$. Calculate

$$v(t) = \dot{x}(t) = \omega X \cos(\omega t + \phi) \tag{3}$$

$$a(t) = \ddot{x}(t) = -\omega^2 X \sin(\omega t + \phi) \tag{4}$$

Sample $x(t)$ with time step h, and denote $x[n] \overset{\triangle}{=} x(nh)$. One is then interested in approximating $\{v(nh)\}$ or $\{a(nh)\}$ based on the sequence $\{x[n]\}$. Two methods, *forward difference* and *central difference*, are considered for approximation of both the velocity (3) and the acceleration (4). Under the forward difference method, the estimates are

$$v_f[n] = \frac{x[n+1] - x[n]}{h} \tag{5}$$

$$a_f[n] = \frac{v_f[n+1] - v_f[n]}{h} = \frac{x[n+2] + x[n] - 2x[n+1]}{h^2} \tag{6}$$

Under the central difference method, the estimates are

$$v_c[n] = \frac{x[n+1] - x[n-1]}{2h} \tag{7}$$

$$a_c[n] = \frac{x[n+1] + x[n-1] - 2x[n]}{h^2} \tag{8}$$

3.1.1 Forward Difference Method. Let $t = nh$ and $\theta = \omega t + \phi$. It then follows that

$$
\begin{aligned}
v_f[n] &= \frac{1}{h}(x[n+1] - x[n]) \\
&= \frac{1}{h}[X \sin(\theta + \omega h) - X \sin(\theta)] \\
&= m_1 \omega X \cos(\theta + \phi_1) \\
&= m_1 \omega X \cos(\omega t + \phi + \phi_1)
\end{aligned} \tag{9}
$$

where $m_1 = \sin(\omega h/2)/(\omega h/2)$, and $\phi_1 = \omega h/2$. Comparing with (3), one can see that not only the magnitude of $v_f[n]$ is scaled from that of $v(nh)$ by m_1, but also its phase differs from that of $v(nh)$ by ϕ_1. Similarly,

$$
\begin{aligned}
a_f[n] &= \frac{x[n+2] + x[n] - 2x[n+1]}{h^2} \\
&= \frac{X}{h^2}[\sin(\theta + 2\omega h) + \sin(\theta) - 2\sin(\theta + \omega h)] \\
&= -m_2 \omega^2 X \sin(\omega t + \phi + \phi_2)
\end{aligned} \tag{10}
$$

where $m_2 = (\sin(\omega h/2)/(\omega h/2))^2$, and $\phi_2 = \omega h$. Therefore, the magnitude of $a_f[n]$ is scaled from that of $a(nh)$ (compare (4)) by m_2, and its phase differs from that of $a(nh)$ by ϕ_2.

3.1.2 Central Difference Method. For the central difference method, one can show

$$
\begin{aligned}
v_c[n] &= \frac{x[n+1] - x[n-1]}{2h} \\
&= \frac{X}{2h}[\sin(\theta + \omega h) - \sin(\theta - \omega h)] \\
&= \frac{\sin(\omega h)}{\omega h} \omega X \sin(\omega t + \phi)
\end{aligned}
$$
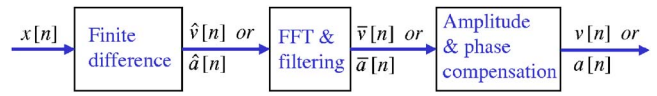
Fig. 3 The three-stage data processing algorithm, applicable to both the forward difference method and the central forward method

$$= \frac{\sin(\omega h)}{\omega h} v(nh) \tag{11}$$

which implies that $v_c[n]$ is in phase with $v(nh)$ but its amplitude is scaled by $\sin(\omega h)/\omega h$. Furthermore, one calculates

$$
\begin{aligned}
a_c[n] &= \frac{x[n+1] + x[n-1] - 2x[n]}{h^2} \\
&= \frac{X}{h^2}[\sin(\theta + \omega h) + \sin(\theta - \omega h) - 2\sin(\theta)] \\
&= -\left(\frac{\sin(\omega h/2)}{\omega h/2}\right)^2 \omega^2 X \sin(\omega t + \phi) = \left(\frac{\sin(\omega h/2)}{\omega h/2}\right)^2 a(nh),
\end{aligned} \tag{12}
$$

which is in phase with $a(nh)$ but with its amplitude scaled.

3.2 The Data Processing Algorithms. The analysis in Sec. 3.1 is based on the assumption that $x[n]$ is sampled from a noiseless sinusoidal signal $x(t)$. This is typically not the case in practice. Nonlinearity associated with the friction induces high-order harmonics in the signals. Furthermore, the position data extracted from the video images is noisy. To deal with these problems, FFT followed by amplitude-based filtering is adopted in compensation. The proposed algorithms consist of three steps (Fig. 3):

1. Stage 1. Finite difference methods. Crude estimates of the velocity and the acceleration are obtained through a plain (forward or central) finite difference method.
2. Stage 2. FFT and amplitude-based filtering. Through FFT, one decomposes the signals obtained from stage 1 into individual frequency components for amplitude/phase compensation (stage 3) and prepares for filtering. Amplitude-based filtering, instead of low-pass filtering, is chosen since the latter may also filter out the high-order harmonics (and thus distort the true frictional dynamics) and introduces extra phase shift to signals. Let M_{max} be the maximum amplitude among all frequency components. Then a frequency component k will be eliminated if its amplitude $M_k \leq \epsilon_0 M_{max}$, where ϵ_0 is chosen based on the noise level.
3. Stage 3. Frequency-dependent compensation. Any remaining frequency component after filtering is compensated in amplitude and phase based on (9) and (10) for the forward difference method, and in amplitude only based on (11) and (12) for the central difference method (as there is no phase distortion). For example, suppose that the forward difference method is adopted and the velocity sequence $\bar{v}_f[n]$ after filtering is

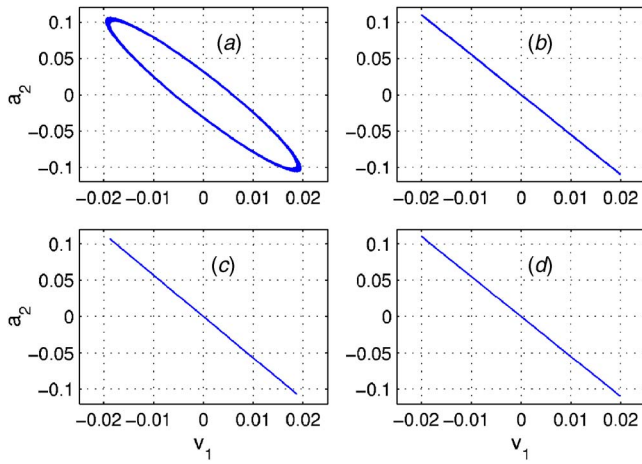$$\bar{v}_f[n] = \sum_k V_k \sin(\omega_k nh + \alpha_k) \tag{13}$$

Then the compensated signal will be

$$v_f[n] = \sum_k \frac{\omega_k h/2}{\sin(\omega_k h/2)} V_k \sin\left(\omega_k nh + \alpha_k - \frac{\omega_k h}{2}\right) \tag{14}$$

Simulation is conducted to test the proposed algorithms. Two sinusoidal trajectories are specified first:

$$x_1(t) = X_1 \cos(\omega t + \pi), \quad x_2(t) = X_2 \sin(\omega t)$$

Fig. 4 Comparison of difference methods: (*a*) forward difference method, (*b*) forward-difference-based three-stage algorithm, (*c*) central difference method, and (*d*) central-difference-based three-stage algorithm

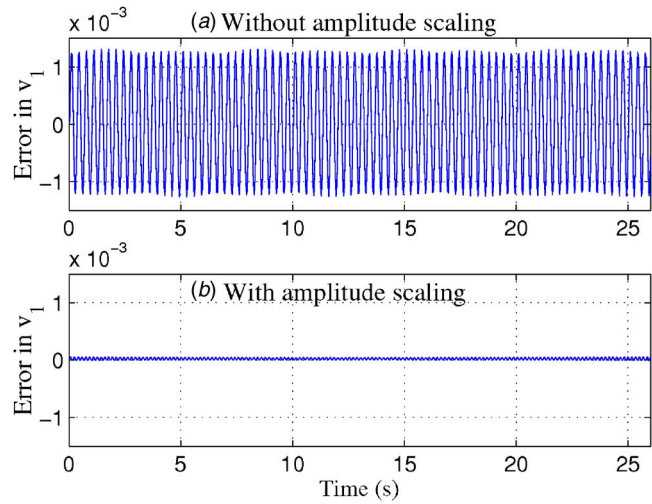Fig. 5 Effect of amplitude compensation on the approximation error

where $x_1(t)$ *mimics* the *relative* position of the slider to the stator, and $x_2(t)$ *mimics* the slider position. One would like to calculate $v_1[n]$ (analogy of relative velocity) and $a_2[n]$ (analogy of acceleration) based on snapshots $x_1[n]$ and $x_2[n]$ with sampling time h. Note that $x_1(t)$ and $x_2(t)$ are specified in such a way that there is a phase difference of π between $v_1(t)$ and $a_2(t)$. In simulation, $X_1 = 0.0011$, $X_2 = 3.1 \times 10^{-4}$, $\omega = 6\pi$, $h = 0.033$, and the filtering level $\epsilon_0 = 0.002$ (although $x_1(t)$ and $x_2(t)$ are purely sinusoidal, one will get extra frequency components in FFT due to the finite number of data points).

Figure 4 compares the a_2 versus v_1 plots obtained through various methods. It is clear that the (plain) forward difference algorithm leads to a spurious loop (Fig. 4(*a*)), introduced by the phase errors in approximating v_1 and a_2. The phase difference between a_2 and v_1 in Fig. 4(*a*) is numerically calculated to be 2.83, which is consistent with the analytical value obtained through (9) and (10). On the other hand, the three-stage algorithms based on either difference method are able to preserve the phase difference of π between a_2 and v_1 correctly (Fig. 4(*b*) and 4(*d*)), and the plots (b) and (d) are nearly indistinguishable. While the plain central difference method is capable of preserving the phase (Fig. 4(*c*)), it induces amplitude distortion. This is evident from Fig. 5, which shows the impact of the amplitude scaling step on the approximation error in v_1 (against the true values) for the central difference method.

4 Empirical Frictional Model

The three-stage algorithm is then used to process the actual position data collected for the microball bearing. In the experiments ten balls were placed in the parallel grooves (five balls on each side), and a 2 g weight was placed on top of the slider to provide additional normal force. Figure 6 shows the trajectories of the stator, the slider, and their relative positions, respectively, extracted from videos taken at 30 frames/second. Note that although the slider experiences slow, random drift due to fabrication-related surface irregularities, its periodic oscillation is dominant. The stator oscillates with frequency 2.95 Hz and amplitude 1.2 mm.

Figure 7 shows the relationships between the slider acceleration a_{slid} (namely, friction normalized by the slider mass) and the relative velocity $v_{slid} - v_{stat}$ when three different schemes are used to compute these quantities. If the plain forward difference method is used following low-pass filtering (cutoff frequency 6 Hz), a loop results (Fig. 7(*a*)), with the phase difference between the fundamental frequency components of a_{slid} and $v_{slid} - v_{stat}$ computed to

be 3.585. However, there are no such loops if one adopts the three-stage processing algorithm based on either the forward difference method (Fig. 7(*b*)) or the central difference method (Fig. 7(*c*)), where the noise tolerance is picked to be $\epsilon_0 = 0.08$. The two plots look identical, with the phase difference on each plot computed to be 3.157 (very close to π). Based on the analysis in Sec. 3, one concludes that the friction is well approximated by a static but nonlinear function of the relative velocity, and the "hysteresis" loop in Fig. 7(*a*) is an artifact of data processing.

From Fig. 7, the friction is almost linear with respect to the relative velocity when the latter is low and, as the magnitude of the relative velocity increases, the friction approaches the maximum value, beyond which it shows a decreasing trend. Simulation will be conducted to further verify the static relationship, and for this purpose, a modified *Langevin* function $\mathcal{L}(\cdot)$ is proposed to approximate the friction versus velocity relationship:

$$F_{fric}(t) = M_{slid}\mathcal{L}(v_{rel}(t)) \qquad (15)$$

where for any q,

$$\mathcal{L}(q) \overset{\triangle}{=} A_0\left(\frac{1}{\alpha q} - \frac{e^{\alpha q} + e^{-\alpha q}}{e^{\alpha q} - e^{-\alpha q}}\right) \qquad (16)$$

To identify the parameters A_0 and α, one calculates
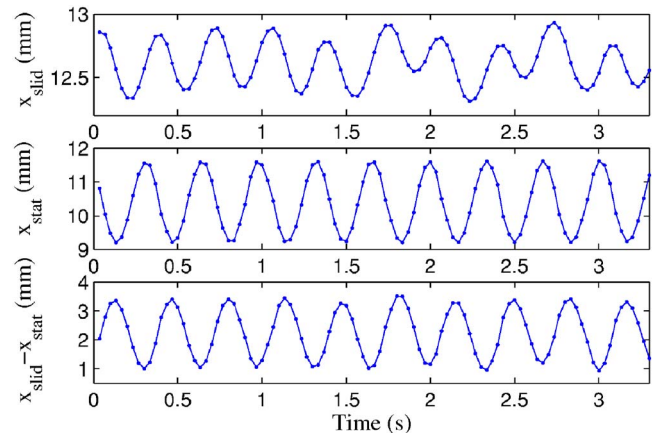
Fig. 6 Experimentally measured trajectories of the slider (top), the stator (center), and their relative position (bottom)
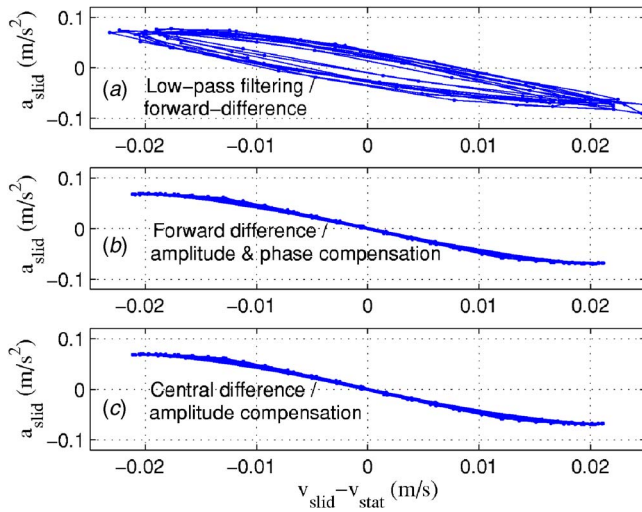
Fig. 7 Slider acceleration (friction) versus relative velocity under different data processing schemes. (*a*) Low-pass filtering followed by forward difference; (*b*) three-stage algorithm based on forward difference; and (*c*) three-stage algorithm based on central difference

Fig. 9 Simulated position trajectories of x_{slid}, x_{stat}, and $x_{slid} - x_{stat}$

$$\frac{d\mathcal{L}(q)}{dq} = \alpha A_0 \left(\frac{4}{(e^{\alpha q} - e^{-\alpha q})^2} - \frac{1}{(\alpha q)^2} \right) \qquad (17)$$

By evaluating the derivatives at $v_{rel} = 0$ and $v_{rel} = 0.015$ in Fig. 7(*c*) and solving (17), the parameters are determined to be $A_0 = 0.112$, $\alpha = 128.65$. Note that the Langevin function is monotonic and thus unable to capture the decreasing trend close to and beyond the largest relative velocity observed in the experiment. This, however, is not a concern considering that the Langevin approximation will be used solely in simulation, and it agrees reasonably well with the experimental data within the velocity range of interest (see Fig. 8).

In the simulation, the equation of motion (2) is integrated using the fourth-order Runge-Kutta method with a time step of 0.001 second, incorporating (1), (15), and (16). The oscillation amplitude of the stator is $X_{stat} = 1.2$ mm and $\omega = 2\pi f_0$ with $f_0 = 2.95$ Hz, both estimated from the experimental data. Figure 9 shows the simulation results, which are in good agreement with the experimental data. Note that the absolute position values are of little relevance since the reference points are defined arbitrarily. The oscillation amplitude of the slider in Fig. 9 is 0.210 mm, while the amplitude of $x_{slid}[n]$ in the experiment (Fig. 6) was 0.206 mm. Furthermore, the phase difference between x_{slid} and x_{stat} in Fig. 9 is 1.384 rad, comparing to 1.416 rad measured in the experiment (Fig. 6).
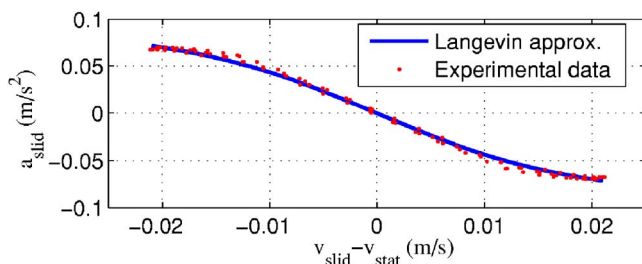
5 A Viscoelastic Model

5.1 The Model. Interactions of all bearing elements, and thus the rolling friction of the bearing, are determined by interactions of the individual balls with the V-grooves. Therefore, it suffices to consider the case of a single ball rolling on a plane. Figure 10 depicts a ball of radius R rolling on a viscous plane with forward velocity v along the x axis. The y axis is defined to point into the paper, while the z axis points upward with $z=0$ representing the plane. If the ball were rigid, it would deform the plane with certain depth of penetration τ' while maintaining its own shape (see the surface represented by the dashed line in Fig. 10). However, for the case of linear microball bearings, the stainless-steel balls and the silicon grooves have close hardness and Young's moduli and thus both should be treated as viscous. One may approximate the deformation of the plane in this case as α times of that for the rigid-ball case, where

$$\alpha = \frac{\mathcal{H}_{ss}}{\mathcal{H}_{ss} + \mathcal{H}_{Si}} \qquad (18)$$

Here $\mathcal{H}_{ss}$ and $\mathcal{H}_{Si}$ represent the hardness of stainless steel and that of silicon, respectively. See the surface represented by the solid line in Fig. 10. We take $\alpha = 0.5$ (thus $\tau' = 2\tau$) considering the comparable hardness values of the contact surfaces.

Let $\mathcal{A}_C$ be the projection of the contact area onto the x-y plane, and (x_c, y_c) be the projection of the sphere center. If the ball were rigid, the z component $z'(x,y)$ of a contact point for $(x,y) \in \mathcal{A}_C$ would satisfy (noting that $z'(x,y) < 0$):

$$[R - \tau' - z'(x,y)]^2 + (x - x_c)^2 + (y - y_c)^2 = R^2$$

which follows from the geometry. Since the ball is viscous, the actual z component $z(x,y) = \alpha z'(x,y) = 0.5z'(x,y)$, resulting in

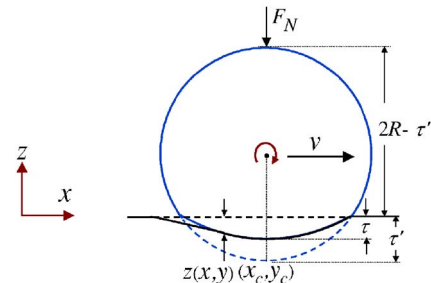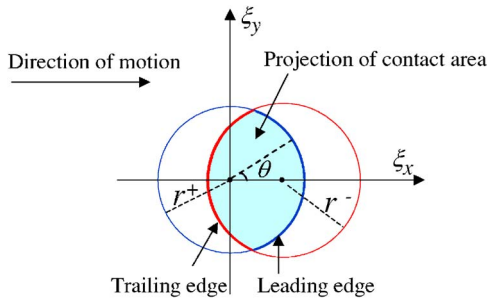Fig. 8 The Langevin approximation to experimental data

Fig. 10 A viscous ball rolling on a viscous plane

Fig. 11 Characterization of the projection $\mathcal{A}_C$ of the contact area

$$[R - 2\tau - 2z(x,y)]^2 + (x - x_c)^2 + (y - y_c)^2 = R^2$$

For $R \gg \tau$, one can approximate $z(x,y)$ by

$$z(x,y) = \frac{(x - x_c)^2 + (y - y_c)^2}{4R} - \tau \qquad (19)$$

Assume that the ball center moves with a constant velocity v, i.e., $\dot{x}_c = v$. The time derivatives of $z(x,y)$ can be computed:

$$\dot{z}(x,y) = -\frac{(x - x_c)v}{2R} \qquad (20)$$

$$\ddot{z}(x,y) = \frac{v^2}{2R} \qquad (21)$$

A system of *independent* mass-spring-damper elements moving in the z direction was used to model the viscoelasticity of the plane by Poschel et al. [28]. This model also applies to the case of bearings described above, where the inertial, elastic, and viscous parameters reflect the properties of *both* the ball and the plane. The force acting on the element at (x,y) is:

$$f(x,y)dxdy = m\ddot{z}(x,y)dxdy + \gamma\dot{z}(x,y)dxdy + kz(x,y)dxdy \qquad (22)$$

where m is the mass of springs per unit area, γ is the damping constant per unit area, and k is the spring constant per unit area. Introducing change of variables $(\xi_x, \xi_y) = (x - x_c, y - y_c)$ and using (20) and (21), one can write (with a bit abuse of notation)

$$f(\xi_x, \xi_y) = (mv^2 - \gamma v \xi_x)/2R + k(\xi_x^2 + \xi_y^2 - 4\tau R)/4R \qquad (23)$$

The projection $\mathcal{A}_C$ of the contact area can be characterized as the intersection of two disks of radii r^+ and r^-, respectively, as illustrated in Fig. 11. The disk of radius r^+ is defined by the geometric condition (19), and thus $r^+ = 2\sqrt{R\tau}$ with center $(0,0)$. The disk of radius r^- is defined by the condition for contact: $f(\xi_x, \xi_y) < 0$, which implies that it is centered at $(\gamma v/k, 0)$ with $r^- = \sqrt{4\tau R + (\gamma^2 - 2mk)v^2/k^2}$. Note that the two disks will overlap for $v = 0$, and, for $v > 0$, the leading edge of $\mathcal{A}_C$ is determined by the geometry (19) while the trailing edge is determined by the condition $f(\xi_x, \xi_y) = 0$.

In addition to the force distribution inside $\mathcal{A}_C$, there is a force distribution along the leading edge $\mathcal{B}$, accelerating the mass elements from 0 to finite velocities in infinitesimal time and contributing to a finite force $F_\mathcal{B}$. This can be calculated as follows. Let θ denote the angular coordinate for elements on the leading edge (Fig. 11); clearly $\theta \in [-\theta_0, \theta_0]$ with $\theta_0 = \cos^{-1}(mv/2\gamma\sqrt{R\tau})$. Within time dt, the leading edge advances vdt along the x direction, and at angle θ a differential mass of $mr^+ d\theta \cdot vdt \cos\theta$ is accelerated from being still to $-\xi_x v/2R = -(v\sqrt{4R\tau}\cos\theta/2R)$. Thus the momentum $dp(\theta)$ received a θ is

$$dp(\theta) = -mr^+ v \cos\theta d\theta dt \cdot \frac{v\sqrt{4R\tau}\cos\theta}{2R}vdt \cos\theta$$

and the differential force is

$$f_\mathcal{B}(\theta)d\theta = \frac{dp(\theta)}{dt} = -2m\tau v^2 \cos^2\theta d\theta \qquad (24)$$

One then evaluates

$$F_\mathcal{B} = \int_{-\theta_0}^{\theta_0} f_\mathcal{B}(\theta)\, d\theta = -m\tau v^2[2\theta_0 + \sin(2\theta_0)]$$

Balancing the forces on the system leads to

$$\int\int_{\mathcal{A}_C} f(\xi_x, \xi_y)d\xi_x\, d\xi_y + F_\mathcal{B} + F_N = 0 \qquad (25)$$

where F_N is the normal force acting on the ball. Given v, (25) is an implicit equation of the penetration depth τ, which can be solved for using a fixed-point algorithm [30].

The rolling friction F_{fric} is then computed from the energy balance equation:

$$F_{fric}v = \int\int_{\mathcal{A}_C} f(\xi_x, \xi_y)\dot{z}(\xi_x, \xi_y)\, d\xi_x d\xi_y + P_\mathcal{B} \qquad (26)$$

where $F_{fric}v$ represents the externally imparted power, the first term on the right-hand side represents the mechanical energy per time imparted into the contact area, and $P_\mathcal{B}$ is the kinetic energy per time transferred to the leading edge:

$$P_\mathcal{B} = \int_{-\theta_0}^{\theta_0} \frac{1}{2}(mr^+ v \cos\theta)\left(-\frac{v\sqrt{4R\tau}\cos\theta}{2R}\right)^2 d\theta$$

$$= \frac{m\tau\sqrt{R\tau}v^3(9\sin\theta_0 + \sin(3\theta_0))}{6R}$$

5.2 Comparison with Experimental Results. The dynamic coefficient of friction (COF)[1] is computed based on the proposed viscoelastic model. In particular, for each velocity v, (25) is solved iteratively for the corresponding penetration depth τ, which is in turn plugged into (26) to evaluate F_{fric}. Although the relative velocity between the slider and the stator varied over time in the experiments, one can assume that the bearing dynamics is at the steady state considering the low velocities involved, and therefore the viscoelastic model is applicable. The overall rolling friction in the bearing is derived from the friction in the single ball-plane interaction.

The following parameters were used in the computation: $m = 1.03 \times 10^{-3}$ kg/m^2, $k = 1.85 \times 10^{18}$ N/m^3, $\gamma = 1.0 \times 10^{14}$ N·s/m^3, $R = 1.43 \times 10^{-4}$ m, and $F_N = 0.002$ N. Here R and F_N were derived from the experimental conditions. The true values of m, k, and γ are difficult to obtain. The m and k values used in calculation were based on the density and modulus values of silicon and steel, assuming 100 nm thick effective elastic layers for the contact surfaces, and γ was chosen to provide reasonable fit to the experimental data (Fig. 12).

Note that the *admissible* values for m, k, and γ are not unique. Indeed, if one obtains m and k by assuming the thickness of the effective elastic layers to be, say, 120 nm instead of 100 nm, and changes γ accordingly, a similar fit to the experimental data is still achievable. The main point here, however, is that the viscoelastic model is able to capture the nonlinear dependence of the rolling friction on the relative velocity that was observed in experiments (see Fig. 7(c)): at relatively low velocities, the friction increases

---

[1]The COF computed from the viscoelastic model will depend on the normal load. The results reported are based on the load used in the experiments.
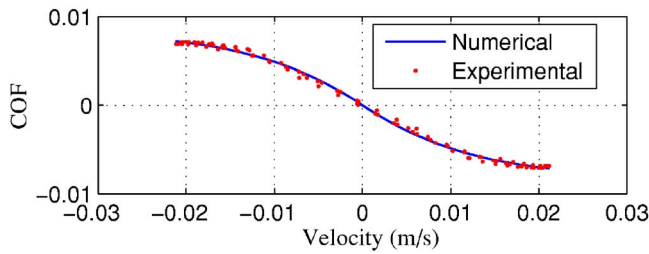
Fig. 12 Computed COF versus experimental measurement

linearly with the velocity; it then approaches the peak value, beyond which it starts to drop. This is more evident from Fig. 13, where the computational results for a larger velocity range are shown.

An intuitive explanation can be provided for the particular way in which the friction varies with the velocity. From (20), the local deformation rate $\dot{z}(\xi_x, \xi_y)$ (and thus the local viscous force density $\gamma \dot{z}(\xi_x, \xi_y)$) is proportional to the velocity v. A dominant portion of the rolling friction comes from the integral of local viscous force density over $\mathcal{A}_C$ (refer to (26)), determined by both the magnitude of the viscous force density and the size of $\mathcal{A}_C$. At low velocities, the elastic force component in f plays a major role in the force balance equation (25) since the viscous component is weak, resulting in a relatively large and constant deformation area $\mathcal{A}_C$. Therefore, the friction rises linearly with v. As v increases, the viscous force term becomes increasingly important in the force balance, and the required contribution from the elastic force term decreases, leading to the reduction of both the contact area and the penetration depth τ (see Fig. 14). Consequently, the overall friction starts to drop. Note that a similar trend was observed and interpreted for the case of a rigid cylinder rolling on a viscous plane [28].

6 Conclusions and Discussions

This paper was focused on the modeling of dynamic friction in MEMS-based linear microball bearings. Novel data processing algorithms were presented to extract the velocity and the force information from the noisy position data. Compensation schemes
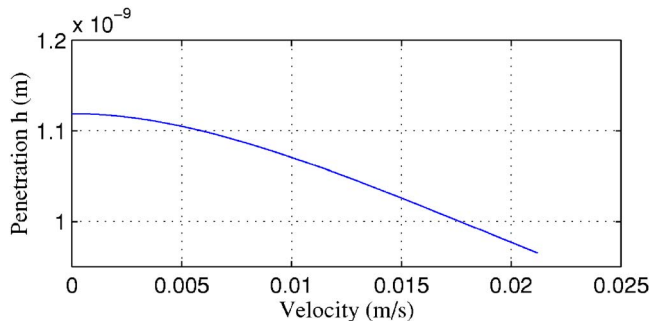

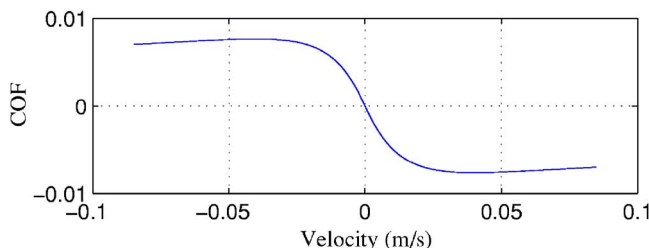**Fig. 13 Computed COF for a larger velocity range**

Fig. 14 Computed penetration depth

were developed for two popular difference methods to eliminate errors in approximating derivative quantities. The approach enabled successful characterization of the rolling friction despite the relatively low video rate used in the experiments. Adopting a higher speed video camera for the measurement would allow one to investigate the frictional behavior at higher relative velocities with lower noise; however, it is expected that the data processing algorithms proposed in this paper will still be applicable.

It was established that the rolling friction versus velocity relationship can be captured by a static (nonlinear), viscous map in the velocity regime examined. Further insight into the contact dynamics was provided by the proposed viscoelastic model. For future work, the findings in this paper will be used in the control of microball bearing-supported micromotors [31] for long-range, high-speed micropositioning.

Although hysteresis was not found to be significant in this study, it could prove important for smaller-scale applications, such as microball bearing-based nanopositioners. The experimental setup in Fig. 2 is inadequate for capturing very fine phenomena such as presliding. In order to study these tribological behaviors, an apparatus will be needed that can perform μN-resolution force excitation/measurement and nm-resolution displacement measurement. Such investigations would provide valuable information complementary to the work in this paper.

References

[1] Mehregany, M., Gabriel, K. J., and Trimmer, W. S. N., 1988, "Integrated Fabrication of Polysilicon Mechanisms," IEEE Trans. Electron Devices, **35**, pp. 719–723.
[2] Kumar, S., and Cho, D., 1990, "A Proposal for Electrically Levitating Micromotors," Sens. Actuators, A, **24**, pp. 141–149.
[3] Frechette, L., Nagle, S. F., Ghodssi, R., Umans, S. D., Schmidt, M. A., and Lang, J. H., 2001, "An Electrostatic Induction Micromotor Supported on Gas-Lubricated Bearings," in *Proceedings of the 14th Annual IEEE International Conference on Microelectromechanical Systems*, August 24–26, Berkeley, CA, pp. 290–293.
[4] Bhushan, B., Israelachvill, J. N., and Landman, U., 1995, "Nanotribology: Friction, Wear and Lubrication at the Atomic Scale," Nature (London), **374**, pp. 607–616.
[5] Sundararajan, S., and Bhushan, B., 2001, "Static Friction and Surface Roughness Studies of Surface Micromachined Electrostatic Micromotors Using an Atomic Force/Friction Force Microscope," J. Vac. Sci. Technol. A, **19**, pp. 1777–1785.
[6] Prasad, R., MacDonald, N., and Taylor, D., 1995, "Micro-instrumentation for Tribological Measurement," in *Proceedings of the 8th International Conference on Solid-State Sensors and Actuators*, June 25–29, Stockholm, Sweden, pp. 52–55.
[7] Miller, S. L., Sniegowski, J. J., LaVigne, G., and McWhorter, P. J., 1996, "Friction in Surface-Micromachined Microengines," in Smart Structures and Materials 1996: Smart Electronics and MEMS, February 26–28, San Diego, CA, Proc. SPIE, **2722**, pp. 197–204.
[8] Tas, N. R., Gui, C., and Elwenspoek, M., 2000, "Static Friction in Elastic Adhesive MEMS Contacts, Models and Experiment," in *Proceedings of the IEEE 13th Annual International Conference on Microelectromechanical Systems*, January 23–27, Miyazaki, Japan, pp. 193–198.
[9] Corwin, A. D., and de Boer, M. P., 2004, "Effect of Adhesion on Dynamic and Static Friction in Surface Micromachining," Appl. Phys. Lett., **84**, pp. 2451–2453.
[10] Ghodssi, R., Denton, D. D., Seireg, A. A., and Howland, B., 1993, "Rolling Friction in a Linear Microstructure," J. Vac. Sci. Technol. A, **11**, pp. 803–807.
[11] Lin, T.-W., Modafe, A., Shapiro, B., and Ghodssi, R., 2004, "Characterization of Dynamic Friction in MEMS-based Microball Bearings," IEEE Trans. Instrum. Meas., **53**(3), pp. 839–846.
[12] Tan, X., Modafe, A., Hergert, R., Ghalichechian, N., Shapiro, B., Baras, J. S., and Ghodssi, R., 2004, "Vision-Based Microtribological Characterization of Linear Microball Bearings," in *Proceedings of ASME/STLE International Joint Tribology Conference*, October 24–27, Long Beach, CA, Paper No. TRIB2004-64334.
[13] Leonard, N., and Krishnaprasad, P. S., 1992, "Adaptive Friction Compensation for Bidirectional Low Velocity Tracking," in *Proceedings of the 31st IEEE Conference on Decision and Control*, December 16–18, Tucson, AZ, pp. 267–273.

[14] Armstrong-Helouvry, B., Dupont, P., and de Wit, C. C., 1994, "A Survey of Models, Analysis Tools and Compensation Methods for the Control of Machines With Friction," Automatica, **30**(7), pp. 1083–1138.

[15] Dahl, P. R., 1968, "A Solid Friction Model," Tech. Rep. No. TOR-158(3107-18), The Aerospace Corporation, El Segundo, CA.

[16] Swevers, J., Al-Bender, F., Ganseman, C. G., and Prajogo, T., 2000, "An Integrated Friction Model Structure With Improved Presliding Behavior for Accurate Friction Compensation," IEEE Trans. Autom. Control, **45**(4), pp. 675–686.

[17] de Wit, C. C., Olsson, H., Astrom, K. J., and Lischinsky, P., 1995, "A New Model for Control of Systems With Friction," IEEE Trans. Autom. Control, **40**(3), pp. 419–425.

[18] Dupont, P., Hayward, V., Armstrong, B., and Altpeter, F., 2002, "Single State Elasto-Plastic Friction Models," IEEE Trans. Autom. Control, **47**(5), pp. 787–792.

[19] Hess, D. P., and Soom, A., 1990, "Friction at a Lubricated Line Contact Operating at Oscillating Sliding Velocities," ASME J. Tribol., **112**, pp. 147–152.

[20] Liang, J. W., and Feeny, B. F., 1998, "Dynamical Friction Behavior in a Forced Oscillator With a Compliant Contact," Trans. ASME, J. Appl. Mech., **65**, pp. 250–257.

[21] Wu, B., Bao, H., Ou, J., and Tian, S., 2005, "Stability and Accuracy Analysis of the Central Difference Method for Real-Time Substructure Testing," Earthquake Eng. Struct. Dyn., **34**, pp. 705–718.

[22] Fornberg, B., 1998, "Calculation of Weights in Finite Difference Formulas," SIAM Rev., **40**(3), pp. 685–691.

[23] Khan, I. R., and Ohba, R., 1999, "Closed-Form Expressions for the Finite Difference Approximations of First and Higher Derivatives Based on Taylor Series," J. Comput. Appl. Math., **107**, pp. 179–193.

[24] Greenwood, J. A., Minshall, H., and Tabor, D., 1961, "Hysteresis Losses in Rolling and Sliding Friction," Proc. R. Soc. London, Ser. A, **259**, pp. 480–507.

[25] Johnson, K. L., 1985, *Contact Mechanics*, Cambridge U. P., Cambridge.

[26] Kalker, J. J., 1990, *Three-Dimensional Elastic Bodies in Rolling Contact*, Kluwer Academic, Dordrecht.

[27] Jiang, Y., Xu, B., and Sehitoglu, H., 2002, "Three-Dimensional Elastic-Plastic Stress Analysis of Rolling Contact," ASME J. Tribol., **124**, pp. 699–708.

[28] Poschel, T., Schwager, T., and Brilliantov, N. V., 1999, "Rolling Friction of a Hard Cylinder on a Viscous Plane," Eur. Phys. J. B, **10**, pp. 169–174.

[29] Peterson, K. E., 1982, "Silicon as a Mechanical Material," Proc. IEEE, **70**(5), pp. 420–457.

[30] Smart, D. R., 1974, *Fixed Point Theorems*, Cambridge U. P., London.

[31] Modafe, A., Ghalichechian, N., Frey, A., Lang, J. H., and Ghodssi, R., 2005, "A Microball-Bearing-Supported Linear Electrostatic Micromotor With Benzocyclobutene Polymer Insulating Layers," in *Proceedings of the 13th International Conference on Solid-State Sensors, Actuators, and Microsystems*, June 5–9, Seoul, South Korea, pp. 693–696.